Journal of Alloys and Compounds 507 (2010) 448–455

Contents lists available at ScienceDirect

Journal of Alloys and Compounds

journal homepage: www.elsevier.com/locate/jallcom

Thermal and mechanical properties of sintered bodies and EB-PVD layers of Y_2O_3 added $Gd_2Zr_2O_7$ ceramics for thermal barrier coatings

Kee Sung Lee[a,*], Kyu Ick Jung[a], Yong Suk Heo[a], Tae Woo Kim[a], Yeon-Gil Jung[b], Ungyu Paik[c]

[a] School of Mechanical Engineering, Kookmin University, 861-1 Chongnungdong, Songbukgu, Seoul 136-702, Republic of Korea
[b] School of Nano & Advanced Materials Engineering, Changwon University, 9 Sarimdong, Changwon, Kyungnam 641-773, Republic of Korea
[c] Department of Energy Engineering, Hanyang University, 17 Haengdangdong, Seongdonggu, Seoul 133-791, Republic of Korea

ARTICLE INFO

Article history:
Received 13 May 2010
Received in revised form 23 July 2010
Accepted 27 July 2010
Available online 4 August 2010

Keywords:
Thermal barrier coatings
Gadolinium zirconate
Yttrium oxide
Thermal conductivity
EB-PVD

ABSTRACT

In this study, the sintered bodies and EB-PVD coatings of gadolinium zirconate ($Gd_2Zr_2O_7$) ceramics with thermal and elastic resistance are prepared by the addition of yttrium oxide (Y_2O_3) to the composition of $Gd_2Zr_2O_7$ for thermal barrier coatings. XRD analysis reveals that the Y_2O_3-doped $Gd_2Zr_2O_7$ thermal barrier material has a thermally stable pyrochlore structure. The Y_2O_3-doped $Gd_2Zr_2O_7$ shows lower thermal conductivity than Y_2O_3-doped stabilized zirconia (YSZ), from 2.12 W/m K to 0.82–1.32 W/m K, and greater hardness than pure $Gd_2Zr_2O_7$, from 6 GPa to 10 GPa as measured by Vickers indentation and more than 20 GPa by nano-indentation, mainly owing to changes in the microstructure. The indentation stress–strain curves and load–penetration depth curves obtained by Hertzian and nano-indentation measurements indicate that the behavior of the curve is crucially influenced by the addition of Y_2O_3 to the pure $Gd_2Zr_2O_7$. The results suggest that Y_2O_3-doped $Gd_2Zr_2O_7$ may be expected to yield hardness and thermal insulation properties superior to those of commercial YSZ coatings for thermal barrier coatings on high temperature alloys.

© 2010 Elsevier B.V. All rights reserved.

1. Introduction

A gas turbine system is operated at high temperatures to increase engine efficiency and improve blade performance. Increased efficiency is closely related to savings in fuel consumption and a reduction in the maintenance cost of cooling [1,2]. The operating temperature of a gas turbine system tends to increase from 1100 °C to 1500°C and is considered one of the most important factors that affect the efficiency of gas turbine-operated power systems. One way of increasing efficiency is to use advanced ceramic materials for the components of hot section parts of alloys. Thermal insulation by a thermal barrier ceramic material having low thermal conductivity is one way of constructing an efficient gas turbine system [1–6].

It is recognized that Y_2O_3-doped zirconia (YSZ) ceramic has been used for the thermal barrier materials of the turbine blade, bucket, and combustion liner owing to its low thermal conductivity, good mechanical strength and the similarity of its thermal expansion coefficient with that of bond coat [1,2]. However, the microstructure of commercial YSZ topcoats, which is usually deposited by air plasma sprayed YSZ, is often inhomogeneous. This unfavorable quality leads to the major cause of topcoat failure [1,7]. Sintering occurs at high temperature and the tetragonal phase of zirconia material precipitates a cubic phase that renders the tetragonal phase transformable to a monoclinic phase [8,9]. Sintering and phase transition-induced volume changes cause stress changes in the topcoat layer, which, in turn, causes the failure of the topcoat layer [10].

Therefore, promising rare earth zirconate ceramics have been suggested as materials for thermal barrier coatings [1–6]. It is reported that zirconate ceramic offers the advantage of having no phase transition during thermal aging and can maintain lower thermal conductivity than YSZ. The Electron Beam Physical Vapor Deposition (EB-PVD) process has been developed to improve the durability of thermal barrier coatings (TBCs) because this process can be used to improve the bonding strength and strain tolerance in place of air plasma TBCs [2,6,11–13]. The process is known to be reliable and strain-tolerant because it can produce TBCs with a unique columnar microstructure at high deposition rates, and can form durable and dense layers containing nano-sized pores, nano-gaps and some feather-like structures [14–16].

However, the mechanical properties of zirconate ceramics are still inferior to those of YSZ. In general, when hard dust and particles come in contact with the topcoat of a gas turbine component, the contact stresses can cause damage on the TBCs. Fatigue stresses by vibration may cause critical stresses in the TBCs. Foreign object damage (FOD) can be also created by large particles on ceramic coatings. Ceramic TBCs are prone to wear when subjected to high

---

[*] Corresponding author. Tel.: +82 2 910 4834; fax: +82 2 910 4839.
E-mail address: keeslee@kookmin.ac.kr (K.S. Lee).

0925-8388/$ – see front matter © 2010 Elsevier B.V. All rights reserved.
doi:10.1016/j.jallcom.2010.07.196

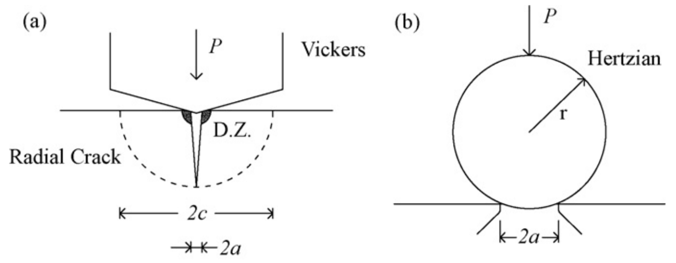

Fig. 1. Schematic diagrams of (a) Vickers indentation and (b) Hertzian indentation.

temperatures for long periods of time, which limits the life of the coating. When the contact force exceeds a critical point or critical fatigue stresses are involved at high numbers of cycles, contact damage can be initiated as deformed inelastic zones or cracks at the critical flaw in highly localized stress fields. Indentation techniques such as Hertzian, Vickers and nano-indentations [17–19] are used to evaluate the damage characteristics of TBC layers in this study. Schematic diagrams of the Vickers and Hertzian indentations used in this study are shown in Fig. 1. A Hertzian contact test using a hard tungsten carbide (WC) ball is used to characterize the elastic and inelastic localized stress–strain curves. Vickers indentation and nano-indentation tests are also used to characterize the hardness of TBCs after inducing localized microsized damage using a diamond indenter.

This work aims to study Y_2O_3, which is added to $Gd_2Zr_2O_7$ ceramics to produce advanced TBCs. These TBCs are required to have better thermal and mechanical properties than existing TBCs such as YSZ and pure $Gd_2Zr_2O_7$ material. In this work, we investigate the effect of Y_2O_3 content on thermal properties such as the thermal expansion coefficient and thermal conductivity, and on mechanical properties such as the hardness, indentation stress–strain curve and load–penetration depth curve of $Gd_2Zr_2O_7$ ceramics. The samples are prepared as relatively dense-sintered materials and EB-PVD coatings. A particular focus of our study is to show the change caused by Y_2O_3 addition on the microstructure, thermal conductivity, hardness and mechanical behaviors of the resultant materials, as reflected in the indentation stress–strain curves and load–penetration depth curves.

2. Experimental procedures

The starting powders for the sintered materials used to characterize the thermal and mechanical properties of thermal barrier materials were Gd_2O_3 (Terio, TGdO-3N, Japan), pure ZrO_2 (Tosoh, TZ-25, Japan) and 3 mol%, 4.56 mol%, 8 mol% and 10 mol% yttria stabilized zirconia (YSZ, Terio, Japan). Pure ZrO_2, 3 mol% YSZ, 4.56 mol% YSZ, 8 mol% YSZ and 10 mol% YSZ added Gd_2O_3 are designated as GZO, 3Y-GZO, 4.56Y-GZO, 8Y-GZO and 10Y-GZO, respectively. The detailed compositions of GZO ($Gd_2Zr_2O_7$) and Y_2O_3-doped $Gd_2Zr_2O_7$ (3Y-GZO, 4.56Y-GZO, 8Y-GZO and 10Y-GZO) are described in Table 1. The powders were ball-milled in ethanol for 24 h. The milled powder was dried and sieved with a 150 μm screen.

Each powder was uniaxially pressed at a pressure of 30 MPa into a 20 mm diameter disc and then sintered in air at 1600 °C for 2 h at the rate of 5 °C/min. The sintered bodies to be used for the evaluation of the thermal and mechanical properties were then machined using diamond paste. The ingot to be used as a porous target material for EB-PVD coating was sintered at 1350 °C for 2 h. An alumina substrate, which is known as the main reaction component between the topcoat and bondcoat alloys, was prepared by polishing the surface of a commercial sintered plate (purity 96%, M.W.F.I, Korea).

Table 1
Compositions of pure $Gd_2Zr_2O_7$ and Y_2O_3-doped sintered $Gd_2Zr_2O_7$.

Material	Gd_2O_3 (wt%)	ZrO_2 (wt%)	Y_2O_3 (wt%)
GZO	59.5	40.5	–
3Y-GZO	57.20	40.5	2.30
4.56Y-GZO	55.98	40.5	3.52
8Y-GZO	53.05	40.5	6.45
10Y-GZO	51.25	40.5	8.25

GZO, 4.56Y-GZO and 8Y-GZO coatings were deposited from the fabricated target ingots onto substrates in vacuum using a 10 kW EB-PVD instrument. The substrate temperature was maintained at 900 °C. The maximum power of the instrument was maintained at 3.75 kW. During deposition, the pressure in the chamber was kept at about 0.013 Pa. The deposition rate was controlled to approximately 0.5 μm/min for a total of <20 min.

The densities of the sintered materials were measured using the Archimedes method. The phases of the sintered products were qualitatively analyzed using an X-ray diffractometer (XRD, D/Max2000-Ultima Plus, Rigaku, Japan). The central part of each specimen was fractured to characterize the microstructure, porosity, size and size distribution of the pores. The microstructure and morphology of the specimens were examined by scanning electron microscopy (SEM, JEOL, JSM-6700F, Japan). The coating surface and fractured surface perpendicular to the coating surface was examined. The porosity of each composition was checked using an image analyzer as well as the Archimedes method. We also used a mercury porosimeter to check the size and size distribution of the pores in each specimen.

The thermal diffusivity, α, was measured using a Laser Flash Apparatus (LFA, NETZSCH, LFA427, Germany) for the GZO, 3Y-GZO, 4.56Y-GZO, 8Y-GZO and 10Y-GZO sintered materials. Both the top and the bottom of the specimens were blackened because YSZ is semi-transparent for a wide range of wavelengths. The laser light was transmitted to one side of the specimen, then, the thermal diffusivity was determined as a function of the time, t, by measuring the temperature change, ΔT, of the specimen using an IR sensor. The thermal diffusivity, α, was calculated using Eq. (1).

$$\alpha = 0.1388 \times \left(\frac{d^2}{t^{1/2}}\right) \tag{1}$$

In Eq. (1), d is the thickness of the specimen and $t^{1/2}$ is the corresponding time at $1/2\ \Delta T_{\max}$ in the t–ΔT graph. For each specimen, we measured the diffusivity three times at the same temperature. The specific heat, C_p, was also measured using a differential scanning calorimeter (DSC). The thermal conductivity, k, was then calculated using Eq. (2).

$$k = \alpha \rho C_p \tag{2}$$

In Eq. (2), ρ is the density of the specimen.

We measured the thermal expansion coefficients of the GZO, 3Y-GZO, 4.56Y-GZO, 8Y-GZO and 10Y-GZO sintered materials for a 5 mm × 5 mm × 25 mm specimen in air, as the temperature of the specimen was changed from room temperature to 1340 °C at a heating rate of 10 °C/min and a cooling rate of 10 °C/min using a dilatometer (L75, LINSEIS, Germany).

Hertzian indention tests were carried out using a tungsten carbide (WC) sphere with a radius of $r = 1.98$ mm on sintered materials and EB-PVD coatings [17,18]. Indentation stress–strain curves were obtained from measurements of the contact radius for various values of P and r, and for loads from 30 N to 4000 N. Then the indentation stress, $p_o = P/\pi a^2$, and indentation strain, a/r were calculated [18,20,21].

Vickers indentation tests were performed using a microhardness tester on the sintered materials. The hardness was measured as a function of the indentation load, P, and the average value of the half-diagonal lengths of each indent, a. The load was varied from 1 N to 10 N.

$$H = \frac{p}{2a^2} \tag{3}$$

Nano-indentations were carried out using a three-sided pyramidal Berkovich diamond indenter on the EB-PVD coating materials. The indentation load was $P = 10$–40 mN, and 10 indentations were made at each load. All indentations were performed using the same load–time schedule, and the load–penetration depth curves were obtained and used to calculate the hardness.

3. Results and discussion

3.1. Sintered materials

3.1.1. Phase and microstructure of sintered materials

X-ray diffraction analysis revealed that all the sintered materials prepared in this study had mainly a pyrochlore structure as shown in Fig. 2. The main peaks at $2\theta = 28°$, $34°$, $49°$ and $58°$ corresponded to the pyrochlore structure. The peaks of Y_2O_3-doped $Gd_2Zr_2O_7$ slightly shifted due to the mismatch of the atomic radius, phase transition or vacancy creation according to the addition of Y_2O_3, so the position of the main peak was not changed, indicating that the doping of Y_2O_3 into the pyrochlore crystal lattice does not change the crystal structure very much. Although studies in the literature show that Gd substitution by smaller lanthanides induces a fluorite structure in pyrochlore [22–24], the resulting structure is considered a pyrochlore–fluorite mixture rather than a complete fluorite structure. Moreover, the radius of Y^{3+} (0.090–0.1019 nm) relative to that of Gd^{2+} (0.094–0.1053 nm) is not much smaller [22]. The ionic

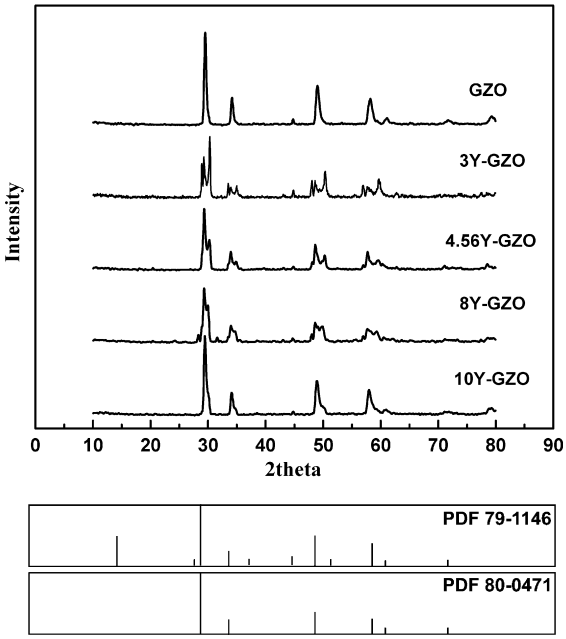

Fig. 2. XRD patterns of the GZO, 3Y-GZO, 4.56Y-GZO, 8Y-GZO and 10Y-GZO sintered materials. Reported XRD patterns are shown as a reference.

radius ratio of Y^{3+}/Zr^{4+} is about 1.45 [23]. Therefore pyrochlore-typed $Gd_2Zr_2O_7$ is comparatively tolerant to Y_2O_3 addition in this study.

The relative densities of the $Gd_2Zr_2O_7$ and Y_2O_3-doped sintered $Gd_2Zr_2O_7$ materials with various compositions that were sintered at the same conditions of 1600 °C for 2 h are shown in the graph of Fig. 3. The densities of the sintered materials were measured, and the calculated relative densities were plotted. The result indicates that 4.56Y-GZO was the most dense-sintered material. The porosity as measured using the Archimedes method is also shown in Table 2. The relative densities of 8Y-GZO and 10Y-GZO are smaller than that of 4.56Y-GZO, corresponding to the increasing porosity of the sintered materials. It is known that a vacancy should be formed [9,25] to maintain electrical neutrality according to the Kröger–Vink relation by Y_2O_3 or Gd_2O_3 doping in a ZrO_2 composition, as indicated in Eqs. (4) and (5).

$$Y_2O_3 \xrightarrow{ZrO_2} Y'_{Zr} + V_0^{\circ} + O_0 \tag{4}$$

Table 2
Porosities of pure $Gd_2Zr_2O_7$ and Y_2O_3-doped sintered $Gd_2Zr_2O_7$.

Material	Porosity (%)
GZO	7.0 ± 0.8
3Y-GZO	1.0 ± 0.8
4.56Y-GZO	0.1 ± 0.05
8Y-GZO	6.0 ± 0.7
10Y-GZO	10.0 ± 0.8

$$Gd_2O_3 \xrightarrow{ZrO_2} 2Gd''_{Zr} + V_0^{\circ\circ} + 3O_0 \tag{5}$$

Therefore, it is conjectured that the newly formed vacancy in the oxygen lattice by Y_2O_3 addition allows atoms to move into an equilibrium position with lower energy thermodynamically, as a result of which material transport readily occurs during sintering by the addition of Y_2O_3 [9]. Therefore, the sintering density increases as the content of the oxygen vacancy increases [26]. Other literature reports that the atomic distance shortens, and the bond energy increases by the increase in the Y_2O_3 concentration in ZrO_2, thus it affects the thermal expansion coefficient [27].

The addition of Y_2O_3 in sintered $Gd_2Zr_2O_7$ material has an influence on the pore size and distribution, as shown in Fig. 4. Pore sizes and their distributions as measured by an Hg porosimeter at the central region of each specimen are plotted in the graph for GZO, 3Y-GZO, 4.56Y-GZO, 8Y-GZO and 10Y-GZO. Note that there are fewer larger pores and that the pores are of more uniform sizes in the 4.56Y-GZO sample than in the GZO or 3Y-GZO sample. It is observed that there are uniform pores with sizes ranging between 80 nm and 140 nm and smaller for the 4.56Y-GZO sample. The diameter of the pores increases and there is a wider size distribution for the 8Y-GZO and 10Y-GZO samples.

The fractured-surface views of the GZO, 3Y-GZO, 4.56Y-GZO, 8Y-GZO and 10Y-GZO materials sintered at 1600 °C for 2 h are shown in Fig. 5. The microstructure was obtained by SEM observation. Note that the relative densities shown in Fig. 3 for GZO, 8Y-GZO and 10Y-GZO are smaller than those of 3Y-GZO and 4.56Y-GZO, corresponding to the increasing porosity in the sintered samples, as shown in the SEM images. As the Y_2O_3 concentration increases, from GZO to 4.56Y-GZO, densification occurs with decreasing porosity, whereas the pore shapes do not change very much. In 3Y-GZO, local densified regions with larger sizes of pores nearby were observed due to the small addition of Y_2O_3, as shown in Fig. 5(b). The locally densified regions were distributed uniformly as the Y_2O_3 concentration increased to 4.56Y-GZO, as shown in

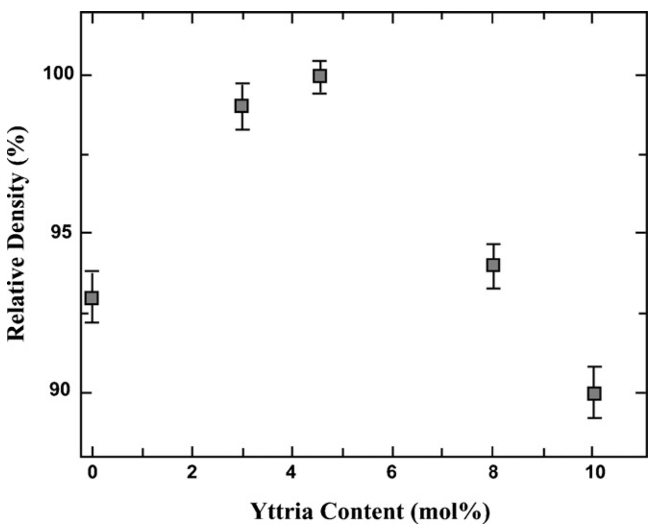

Fig. 3. Relative densities of pure $Gd_2Zr_2O_7$ and Y_2O_3-doped sintered $Gd_2Zr_2O_7$.

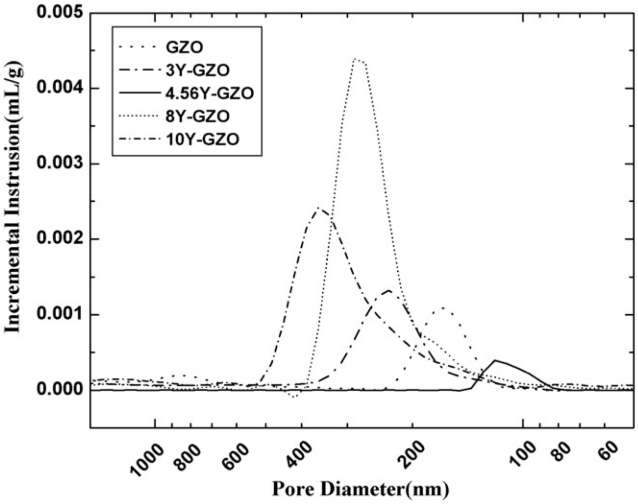

Fig. 4. The result of pore size analysis by Hg porosimeter in pure $Gd_2Zr_2O_7$ and Y_2O_3-doped sintered $Gd_2Zr_2O_7$.

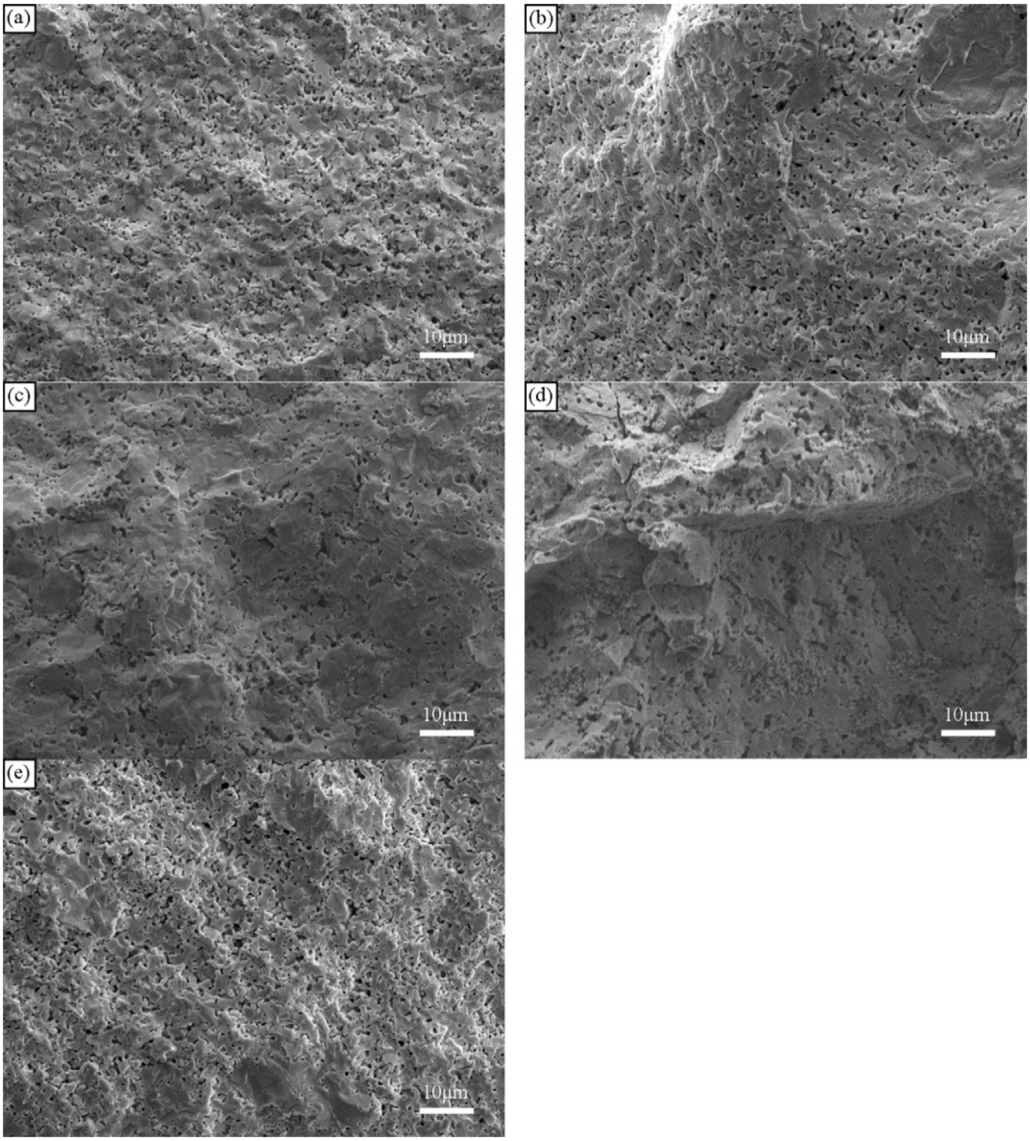

Fig. 5. SEM images of the fractured surface of (a) GZO, (b) 3Y-GZO, (c) 4.56Y-GZO, (d) 8Y-GZO and (e) 10Y-GZO sintered materials.

Fig. 5(c). As the Y_2O_3 concentration increases, from 4.56Y-GZO to 10Y-GZO, the porosity increases again even though locally densified regions occur. The SEM images also reveal that the fractured surfaces are irregular for 3Y-GZO, 4.56Y-GZO and 8Y-GZO, while the surfaces of GZO and 10Y-GZO are relatively flat.

3.1.2. *Thermal properties of sintered materials*

Plots of the thermal expansion coefficients for the $Gd_2Zr_2O_7$ and Y_2O_3-doped sintered $Gd_2Zr_2O_7$ materials with various Y_2O_3 compositions versus temperature are shown in Fig. 6. YSZ data are inserted in the graph from the previous literature [1]. In general current thermal barrier coatings consist of three layers: a Ni-based substrate layer, an oxidation-resistant bondcoat layer and a ceramic topcoat layer. In this layered system, the thermal expansion coefficient is an important property because thermal stress due to the thermal expansion mismatch between the TBCs and the bond coat layer may cause the failure of the TBCs [7]. Because the thermal expansion coefficient of the commercial bond coat material, NiCoCrAlY, is about $17.5 \times 10^{-6}/^{\circ}C$ (room temperature ~1000 °C), [1] a larger thermal expansion of the TBC means a lower thermal mismatch between the bond coat and the topcoat layer. A high thermal expansion coefficient does not build up residual tensile stress by

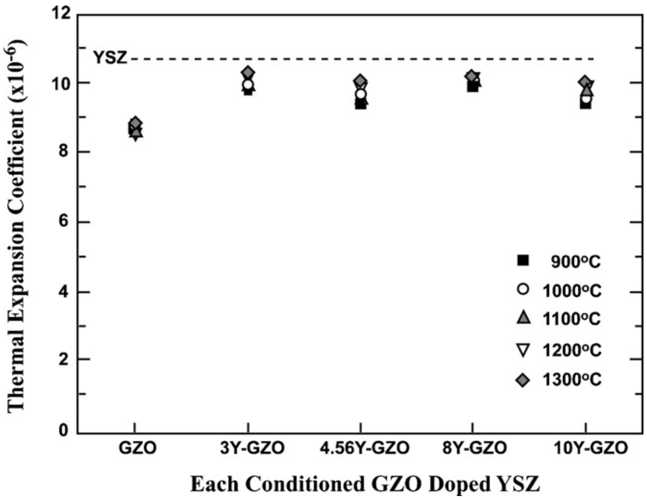

Fig. 6. The curves of thermal expansion of pure $Gd_2Zr_2O_7$ and Y_2O_3-doped sintered $Gd_2Zr_2O_7$.

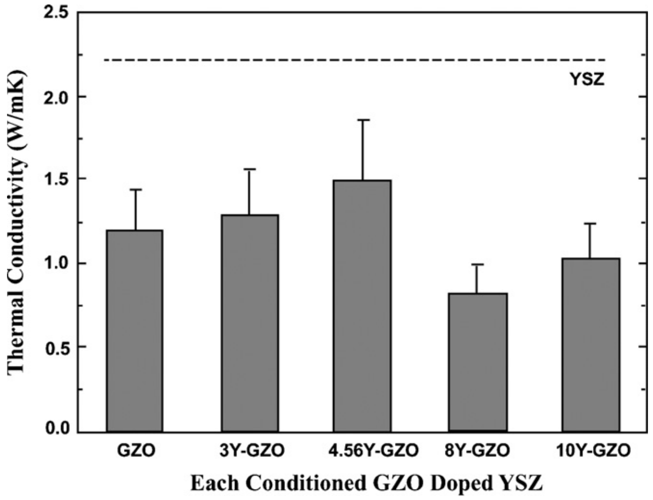

Fig. 7. The curves of thermal conductivity for pure $Gd_2Zr_2O_7$ and Y_2O_3-doped sintered $Gd_2Zr_2O_7$.

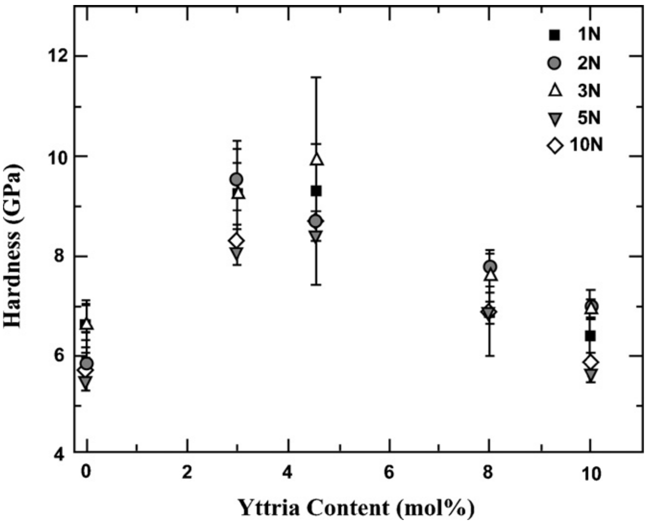

Fig. 8. The variation of the hardness behavior with the addition of Y_2O_3 to sintered $Gd_2Zr_2O_7$.

thermal mismatch between the topcoat and the bondcoat layer during repetitive heating and cooling cycles. The data in Fig. 6 show that the addition of Y_2O_3 almost increases the thermal expansion coefficient of $Gd_2Zr_2O_7$ to that of YSZ at temperatures above 900 °C. It is notable that the thermal expansions of Y_2O_3-doped $Gd_2Zr_2O_7$ are similar and that the highest value, $10–10.5 \times 10^{-6}/°C$ at high temperature, >1200 °C, is close to that of YSZ, $10.7 \times 10^{-6}/°C$. On the other hand, the thermal expansion coefficient of $Gd_2Zr_2O_7$ ($9 \times 10^{-6}/°C$) indicates that it causes a larger thermal expansion mismatch with bondcoat during thermal cycling and cooling. Thus, it is expected that Y_2O_3-doped $Gd_2Zr_2O_7$ can be stably used even at high temperature.

Fig. 7 shows the thermal conductivity versus Y_2O_3 composition for the $Gd_2Zr_2O_7$ and Y_2O_3-doped sintered $Gd_2Zr_2O_7$ materials. The thermal conductivity is also an important property for determining the thermal insulation capacitance of TBCs [28]. It is noteworthy that all GZO zirconate materials show lower thermal conductivities relative to those of YSZ ($\cong 2.1 \sim 2.2$ W/m K). Although the thermal conductivities of 3Y-GZO and 4.56Y-GZO are higher than that of GZO, the values are still lower than that of YSZ as reported in the literature [1]. The results of the thermal conductivity of Y_2O_3-doped $Gd_2Zr_2O_7$, as shown in Fig. 7, were obtained from the results of the change in the porosity and vacancy by the addition of Y_2O_3 in the $Gd_2Zr_2O_7$ material. The thermal conductivities of 3Y-GZO and 4.56Y-GZO were a little higher than that of GZO mainly due to the high relative density (lower porosity), as shown in Figs. 3–5. However, in the case of 8Y-GZO, the effect of increased vacancy concentration is dominant in the reduction of the thermal conductivity of GZO. The vacancy created from the addition of yttrium oxide to maintain electrical neutrality [25] contributes to phonon scattering. It is conjectured that the slightly higher thermal conductivity of 10Y-GZO relative to that of 8Y-GZO is due to vacancy clustering that results from the interaction of vacancies [28].

3.1.3. *Mechanical properties of sintered materials*

The hardness as measured by Vickers indentation is shown in Fig. 8 for the $Gd_2Zr_2O_7$ and Y_2O_3-doped sintered $Gd_2Zr_2O_7$ materials for various indentation loads as a function of Y_2O_3 addition. Note that the hardness of 3Y-, and 4.56Y-GZO, 10 GPa, is greater than that of GZO, 6 GPa. The hardness of 8Y-GZO is also greater than those of the GZO materials, corresponding to the contribution of the addition of Y_2O_3 to hardness improvement.

Hertzian indentation stress–strain curves of the $Gd_2Zr_2O_7$ and Y_2O_3-doped sintered $Gd_2Zr_2O_7$ materials are plotted in Fig. 9. The results of the indentation stress–strain curve show that GZO is indicative of a relatively plastic material (close to 0.5 at high strain range). On the other hand, 4.56Y-GZO is a stiffer material and exhibits an elastic property (strain hardening coefficient, $\alpha \cong 1$ even at high strain range) despite the fact that all damages observed in this study are quasi-plastically deformed damages [18]. It is expected that a higher elastic modulus and yield stress would contribute to high resistance to damage from particle attacks or wear during gas turbine operation when the TBCs are not subject to critical failure conditions caused by TGO formation. It is also notable that the tendency of the stiffness change of each GZO material is related to the porosity as shown in Table 2 and Figs. 3–5. As the indentation stress–strain curve of 4.56Y-GZO is similar to that of YSZ [21,29], we can say that the mechanical properties of GZO material are made comparable to those of commercial YSZ by the addition of Y_2O_3.

3.2. *Coating materials*

3.2.1. *Phase and microstructure of coating materials*

The results of X-ray diffraction reveal that all coating layers deposited by EB-PVD also consist of pyrochlore structure. All phases

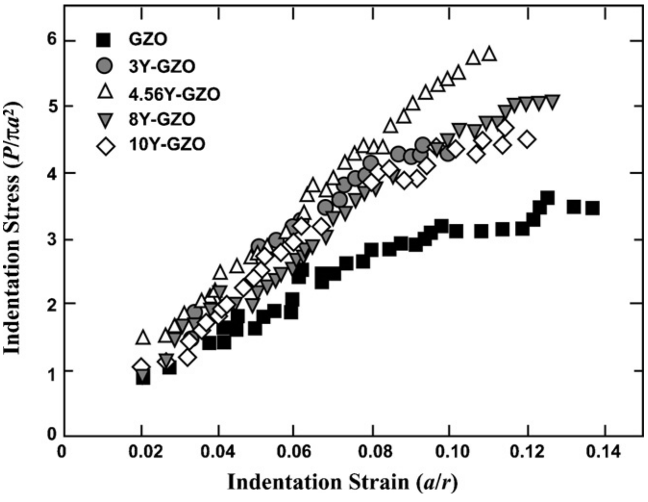

Fig. 9. The Hertzian indentation stress–strain curves for pure $Gd_2Zr_2O_7$ and Y_2O_3-doped sintered $Gd_2Zr_2O_7$.

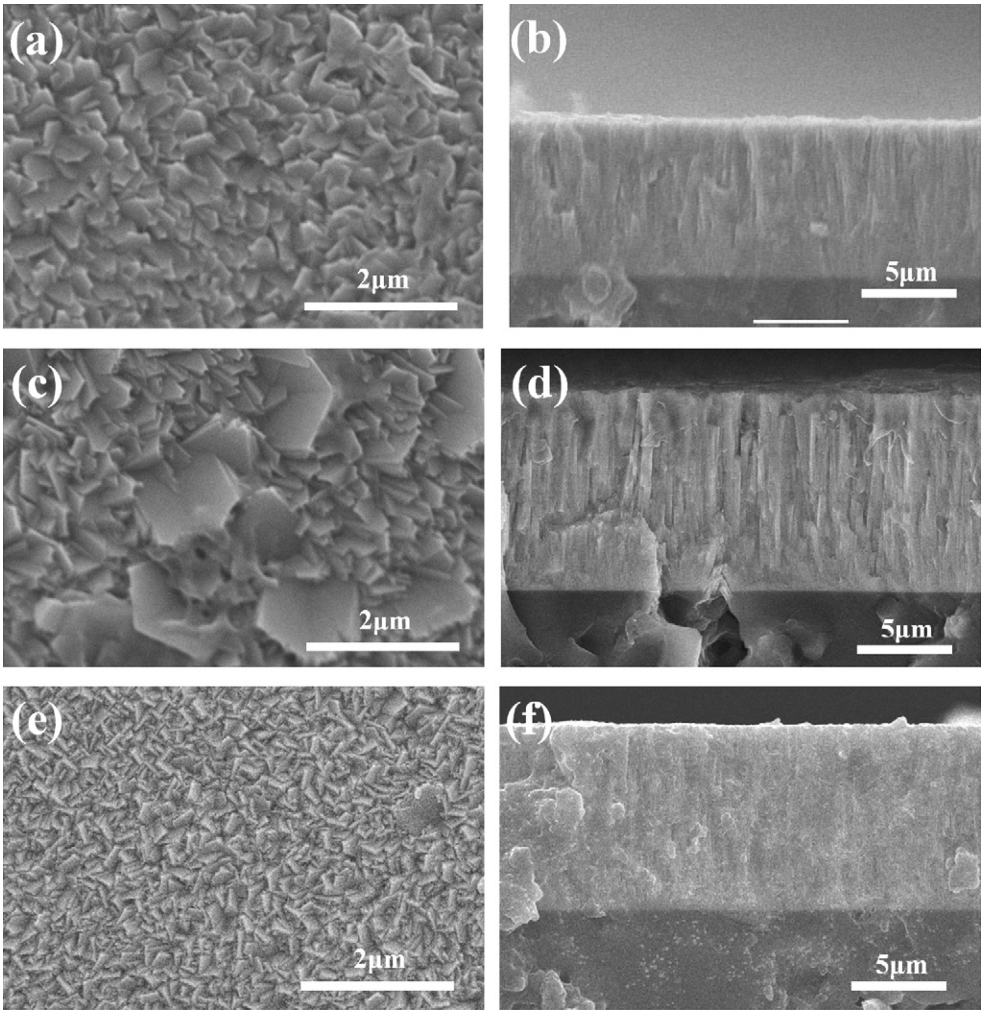

Fig. 10. SEM micrographs of TBCs deposited by EB-PVD and, GZO, showing the morphology at (a) the coating surface and (b) the fractured surface, where (c) and (d) are for 4.56Y-GZO, and (e) and (f) are for 8Y-GZO coatings.

of GZO correspond to the pyrochlore structure, except the Al_2O_3 phase, which was used as the substrate material. On the other hand, the peaks of Y_2O_3-added $Gd_2Zr_2O_7$ showed a little shift due to the mismatch of the atomic radius and conversion to fluorite structure, but most of the peaks indicate the doping of Y_2O_3 into the pyrochlore crystal lattice, as do the sintered materials shown in Fig. 2.

The SEM microstructures of the coating and fractured surface of the GZO, 4.56Y-GZO, and 8Y-GZO coating layers deposited by EB-PVD are shown in Fig. 10. As the Y_2O_3 concentration increased, from GZO to 4.56Y-GZO, the grains became coarse with abnormal grain growth, but most of the GZO grains remained fine. The images also reveal that the grains are faceting for 4.56Y-GZO and faceting even more for the finer grains of 8Y-GZO, but the average fine-grain sizes of the two samples are similar to each other.

The columnar microstructures of all three samples, GZO, 4.56Y-GZO, and 8Y-GZO, are shown in the cross-sectional views in Fig. 10. However, the columns deposited from the 4.56Y-GZO ingots are clearer, compared to GZO or 8Y-GZO, as shown in the figure. The microstructures in Fig. 10(c) and (d) illustrate that more densification occurred in the case of 4.56Y-GZO, which indicates that the same densification behavior was found in the coating materials as in the sintered materials. Grain growth with densification in Fig. 10(c) and the clearly shown nano-gap in Fig. 10(d) indicate that more densification occurred for 4.56Y-GZO.

The measured density and results of pore analysis show that all coating layers consist of a fully-dense deposition layer (>99.95% of relative density) with a nanometer range of pore sizes. Dense films of about 10 μm thickness are clearly shown in Figs. 10(b), (d) and (f).

3.2.2. *Mechanical properties of coating materials*

Fig. 11 shows Hertzian indentation stress–strain curves of $Gd_2Zr_2O_7$ and Y_2O_3-doped $Gd_2Zr_2O_7$ coatings deposited by EB-PVD. At the same stress condition, the strain of 4.56Y-GZO is smaller than that of GZO or 8Y-GZO, indicating that 4.56 Y-GZO is more elastic than GZO even though all the observed damages are quasi-plastically deformed damages [18]. It is thought that the denser microstructure found in 4.56Y-GZO as shown in Figs. 10(c) and (d) results in harder and more elastic behavior. As a result, it is notable that the indentation stress–strain curve of 4.56Y-GZO is similar to that of YSZ [29]. The results are coincident with those of sintered materials as shown in Fig. 9, indicating that the Y_2O_3 effect also dominates in EB-PVD coating materials.

Fig. 12(a) shows the load–penetration depth curves for GZO and 4.56Y-GZO EB-PVD coatings during nano-indentation. The curve formed by the 4.56 mol% (8 wt%) YSZ data under the same indentation condition is inserted for comparison. At the same load condition, the indentation depth of 4.56Y-GZO is smaller, indicating that 4.56Y-GZO is harder than GZO and YSZ. Our previous result

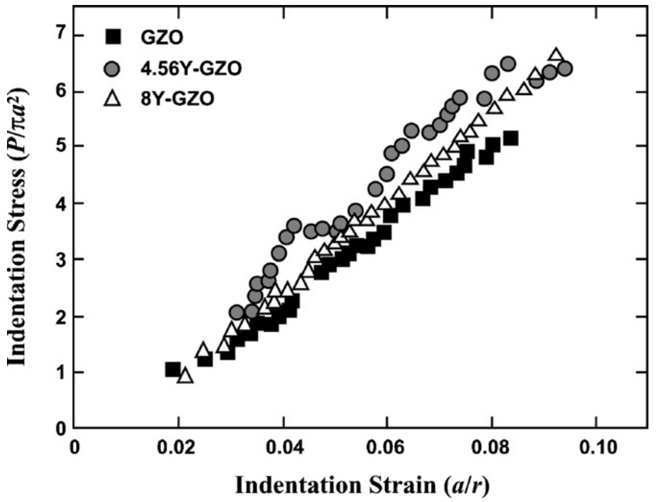

Fig. 11. The Hertzian indentation stress–strain curves for pure $Gd_2Zr_2O_7$ and Y_2O_3-doped $Gd_2Zr_2O_7$ EB-PVD coatings.

relating to the indentation size effect [15] indicates that the coarser and denser columns found in Figs. 10(c) and (d) decrease the probability of the nano-sized indenter being situated on a weak interface between columns, which results in harder behavior.

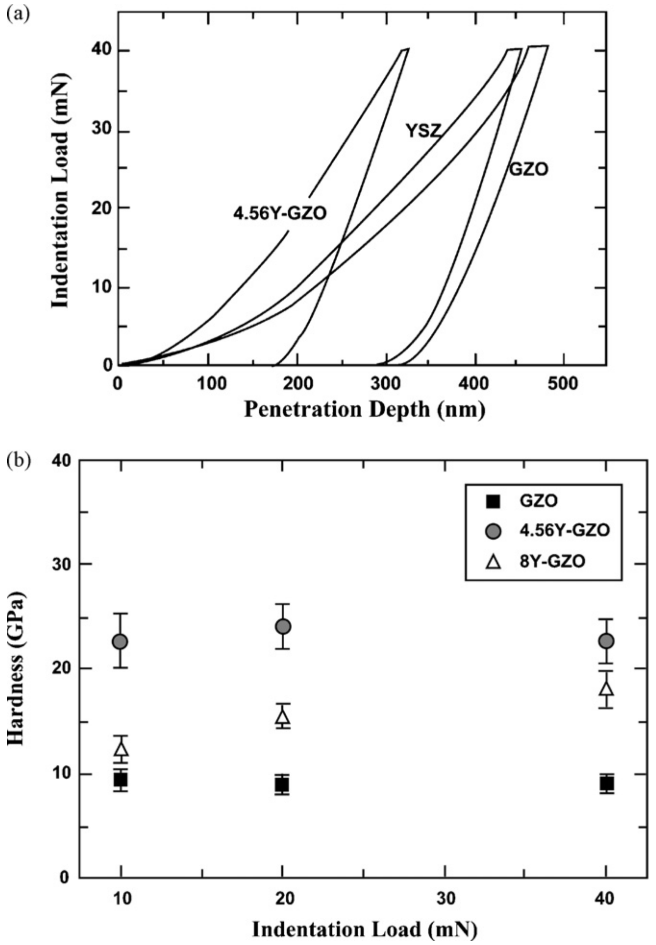

Fig. 12. (a) Load–penetration depth curves of nano-indentation for pure $Gd_2Zr_2O_7$ and Y_2O_3-doped $Gd_2Zr_2O_7$ EB-PVD coatings. The corresponding curve for YSZ is inserted in the graph and (b) hardness calculated from load–penetration depth curves of the nano-indentation test for pure $Gd_2Zr_2O_7$ and Y_2O_3-doped $Gd_2Zr_2O_7$ coatings. The indentation loads are varied from 10 mN to 40 mN.

The hardness is calculated as a function of the load from the load–penetration depth curve of nano-indentation and then plotted, as shown in Fig. 12(b). Note that the hardness increases more at 4.56Y-GZO than for GZO. The plots show that the hardness of EB-PVD coatings is insensitive to the indentation loads. Note that the hardness evaluated by nano-indentation showed higher mechanical properties than that by Vickers indentation, based on a comparison between Figs. 8 and 12, which indicates the size effects of indentation sites.

In this study we have suggested that microstructure tailoring by Y_2O_3 addition can have an influence on the thermal properties such as thermal conductivity and thermal expansion, and mechanical properties such as hardness, indentation stress–strain curves and load–penetration depth curves in $Gd_2Zr_2O_7$ ceramics. Table 2 and Fig. 5 show that the porosity is changed by the addition of Y_2O_3 to GZO materials. Fig. 4 shows the changes in the pore size and size distribution of GZO by Y_2O_3 addition. Fig. 10 suggests that the densification behavior is changed by Y_2O_3 addition to GZO EB-PVD coating materials.

These results indicate that the tendency of microstructural change is closely related to the tendency of the changes in the thermal properties, as shown in Figs. 6 and 7, and is also closely related to the mechanical properties, as shown in Figs. 8, 9, 11 and 12. Among the tested materials, the 4.56Y-GZO material shows good hardness and an appropriate thermal expansion coefficient while maintaining a lower thermal conductivity than the YSZ material. A similar behavior of the indentation stress–strain curve for Y_2O_3-doped $Gd_2Zr_2O_7$ EB-PVD coatings relative to sintered materials indicates that the mechanical resistance can be improved by the addition of Y_2O_3 in $Gd_2Zr_2O_7$ for thermal barrier coatings.

4. Conclusions

In this study, Y_2O_3 from 2.3 wt% to 8.25 wt% was added to $Gd_2Zr_2O_7$, to improve the thermal and elastic properties of a pure $Gd_2Zr_2O_7$ thermal barrier material. Mechanical properties such as the hardness, stress–strain curves and load–penetration curve as measured by indentation tests were evaluated. Thermal properties such as the thermal expansion coefficient and thermal conductivity were evaluated for pure $Gd_2Zr_2O_7$ and Y_2O_3-doped sintered $Gd_2Zr_2O_7$ materials. The results of phase analysis of the Y_2O_3-doped $Gd_2Zr_2O_7$ confirmed the thermally stable pyrochlore structure of the material.

Mechanical properties such as the hardness and elastic properties were enhanced in $Gd_2Zr_2O_7$ by Y_2O_3 addition mainly because of microstructural change that resulted from change in the densification behavior. The hardness was improved from 6 GPa to 10 GPa as measured by Vickers test and more than 20 GPa as measured by nano-indentation test with the addition of 3.52 wt% Y_2O_3 (4.56 mol% of YSZ to Gd_2O_3) to $Gd_2Zr_2O_7$.

The Y_2O_3-doped $Gd_2Zr_2O_7$ showed lower thermal conductivity than YSZ, from 2.12 W/m K to 0.82–1.32 W/m K and the increase of Y_2O_3 content in the $Gd_2Zr_2O_7$ composition enhanced the thermal expansion coefficient of the pure $Gd_2Zr_2O_7$, 10–10.5 $\times 10^{-6}/^{\circ}C$.

Acknowledgements

This work was supported by the Power Generation & Electricity Delivery and Human Resources Development of the Korea Institute of Energy Technology Evaluation and Planning (KETEP) grants funded by the Korea Government Ministry of Knowledge Economy (R-2007-1-003-02/2009T100200025 and 2007-P-EP-HM-E-02-0000).

References

[1] X.Q. Cao, R. Vassen, D. Stöver, J. Eur. Ceram. Soc. 24 (2004) 1–10.
[2] Z. Xu, L. He, X. Zhong, R. Mu, S. He, X.Q. Cao, J. Alloy Compd. 478 (2009) 168–172.
[3] Z. Hong-song, X. Qiang, W. Fu-chi, L. Ling, W. Yuan, C. Xiaoge, J. Alloy Compd. 475 (2009) 624–628.
[4] X.Q. Cao, J. Li, X. Zhong, J. Zhang, Y. Zhang, R. Vassen, D. Stöver, Mater. Lett. 62 (2008) 2667–2669.
[5] N.P. Bansal, D. Zhu, Mater. Sci. Eng. A 459 (2007) 192–195.
[6] U. Schulz, B. Saruhan, K. Fritscher, C. Leyens, Int. J. Appl. Ceram. Technol. 1 (2005) 302–315.
[7] A.G. Evans, J.W. Hutchinson, Surf. Coat. Technol. 201 (2007) 7905–7916.
[8] L.Y. Liu, R. Shangkar, P. Howard, Surf. Coat. Technol. 204 (2010) 3154–3160.
[9] K.S. Lee, S. Lee, J.H. Yu, D.W. Seo, S.K. J. Woo, Solid State Electrochem. 11 (2007) 1295–1301.
[10] Z. Xu, L. He, R. Mu, X. Zhong, Y. Zhang, J. Zhang, X. Cao, J. Alloy Compd. 473 (2009) 509–515.
[11] R.G. Wellman, J.R. Nicholls, Tribol. Int. 41 (2008) 657–662.
[12] Z. Xu, L. He, R. Mu, S. He, X.Q. Cao, J. Alloy Compd. 492 (2010) 701–705.
[13] S. Guo, Y. Kagawa, Ceram. Int. 32 (2006) 263–270.
[14] B.K. Jang, H. Matsubara, Mater. Lett. 59 (2005) 3462–3466.
[15] S.H. Park, S.K. Kim, K.S. Lee, J. Philos. Mag. 86 (2006) 5453–5463.
[16] U. Schulz, K. Fritscher, A. Ebach-Stahl, Surf. Coat. Technol. 203 (2008) 449–455.
[17] B.R. Lawn, T.R. Wilshaw, J. Mater. Sci. 10 (1975) 1977–1994.
[18] B.R. Lawn, J. Am. Ceram. Soc. 81 (1998) 1977–1994.
[19] B.R. Lawn, Fracture of Brittle Solids, second ed., Cambridge University Press, Cambridge, UK, 1993.
[20] K.S. Lee, S. Wuttiphan, X.Z. Hu, S.K. Lee, B.R. Lawn, J. Am. Ceram. Soc. 81 (1998) 571–580.
[21] J.Y. Kwon, J.H. Lee, H.C. Kim, Y.G. Jung, U. Paik, K.S. Lee, Mater Sci. Eng. A. 429 (2006) 173–180.
[22] J.A. Diaz-Guillen, A.F. M. Fuentes, R. diaz-Guillen, J.M. Almanza, J. Santamaria, C. Leon, J. Power Sources 186 (2009) 349–352.
[23] Z.G. Liu, J.H. Ouyang, Y. Zhou, J. Li, X.L. Xia, J. Eur. Ceram. Soc. 29 (2009) 647–652.
[24] L. Minervini, R.W. Grimes, J. Am. Ceram. Soc. 83 (2000) 1873–1878.
[25] S. Lee, K.S. Lee, S.K. Woo, J.W. Kim, T. Ishihara, D.K. Kim, Solid State Ionics 158 (2003) 287–296.
[26] S.Y. Yang, J.H. Lee, J.J. Kim, J.S. Lee, Solid State Ionics 172 (2004) 413–416.
[27] H. Hayashi, T. Saitou, N. Maruyama, H. Inaba, K. Kawamura, M. Mori, Solid State Ionics 176 (2005) 613.
[28] W.D. Callister, Materials Science and Engineering an Introduction, fifth ed., Wiley Press, 2000.
[29] K.I. Jung, S.H. Park, J.H. Kim, D.K. Kim, U. Paik, K.S. Lee, Solid State Phenom. 124–126 (2007) 1349–1352.